Tutora

Dra. Lourdes Mestres Vila
*Departament de Química Inorgànica i
Química Orgànica*

Secció de Química Inorgànica

Grau de Química

Treball Final de Grau

Field-assisted sintering: flash sintering

Sinterització assistida per camp elèctric: flash sintering

Lluís Vilella Piqué
June 2020

UNIVERSITAT DE BARCELONA

B:KC Barcelona Knowledge Campus
Campus d'Excel·lència Internacional

Nothing in life is to be feared, it is only to be understood. Now is the time to understand more, so that we may fear less.

Marie Curie

Foremost, I would like to express my sincere gratitude to Dra. Lourdes Mestres who encouraged me to my highest potential and her exemplary guidance and support helped me throughout the whole project. Besides, I would like to thank the rest of lab partners working in the QES group for their assistance and insightful comments.

REPORT

CONTENTS

1. SUMMARY

Flash sintering is a novel technique used for ceramics densification by means of heating and applying an electric field. Its advantages over conventional sintering have been discussed in the present work, amongst which, the following advantages are displayed: energy savings, shorter sintering times and preparation of ceramic materials with complex compositions by controlling abnormal grain growth and stoichiometry, as the loss of volatile compounds is avoided.

The setup for flash sintering has been constantly developing since the introduction of the technique and sophisticated setups have been designed in order to collect all the required data during the same analysis.

Moreover, the electrical response has been reviewed during this process where power, applied field and current are controlled.

Flash sintering mechanisms have also been discussed as various authors proposed different mechanisms to explain this phenomenon such as Joule heating, nucleation of Frenkel pairs and electrochemical reduction.

Furthermore, an extensive list of parameters controlling flash sintering have been studied and its optimization have been discussed; for instance, applied electric field, current density, initial particle size, green density, addition of sintering aids and the atmosphere.

In this work, a comprehensive study of different prediction models have been made. These models have been created to predict sample temperature from furnace temperature, and onset temperature depending on the applied field.

The last bibliographic section exhibit new materials sintering by flash sintering. Dwelling time and temperature are compared with the conventional sintering of the same materials. Useful information can be extracted from this analysis in order to prepare dense ceramics as a few studies about materials' properties show similar results to conventionally sintered materials. However, flash sintering have been shown to substantially reduce onset temperatures and dwelling times.

Concerning the experimental part, conventional sintering and flash sintering experiments of a commercial sample of $BaTiO_3$ have been performed but relative densities and characterization methods have not been carried out due to the pandemic. Regarding the study of a previously prepared $Nd_2Zr_2O_7$, conventional sintering was performed and the resulting relative density was calculated. X-ray diffraction analysis was carried out and the resulting diffractometer was analyzed. Impedance spectroscopy was carried out, but results were not analyzed as a full set of measurements was not performed.

2. RESUM

El *flash sintering* és una innovadora tècnica que permet la densificació de ceràmiques mitjançant tractament tèrmic i l'aplicació d'un camp elèctric. En aquest treball es mostren els seus avantatges respecte a la sinterització convencional: estalvi en l'energia i en el temps de sinterització, possibilitat de preparar materials ceràmics amb composicions complexes, bon control del creixement de gra així com de l'estequiometria, ja que s'eviten les pèrdues de compostos volàtils.

El muntatge experimental pel *flash sintering* s'ha anat desenvolupant de forma constant des de la introducció de la tècnica i s'han dissenyat muntatges cada vegada més complexos que permeten obtenir totes les dades experimentals en un sol anàlisi. En tots els casos es controla la potència, camp aplicat i la intensitat de corrent i s'analitza la resposta elèctrica del material i la contracció que experimenta.

En la bibliografia s'han trobat propostes de diferents autors sobre els mecanismes que permeten explicar el *flash sintering*, com són l'efecte Joule, la nucleació de parells de Frenkel i la reducció electroquímica.

Altrament, s'ha estudiat una llista extensa de paràmetres que controlen el *flash sintering*; per exemple, el camp elèctric aplicat, la densitat de corrent, la mida de partícula inicial, la densitat inicial de la pols compactada, incorporació d'additius i l'atmosfera en la qual es duu a terme la sinterització.

En aquest treball també es presenten els diferents models que permeten predir la temperatura de la mostra, partint de la temperatura del forn, i la temperatura de l'inici del flash, en funció del camp elèctric aplicat.

En la part final de la cerca bibliogràfica es mostren els diferents materials sinteritzats per *flash sintering* i es comparen temps i temperatura del procés amb els valors corresponents als dels mateixos materials sinteritzats de forma convencional. Aquesta informació pot resultar molt interessant de cara a preparar ceràmiques denses mitjançant *flash sintering* per l'estudi de les seves propietats, ja que els pocs estudis que hi ha mostren que s'obtenen propietats molt

semblants a les ceràmiques sinteritzades de forma convencional, però amb una reducció molt important de la temperatura i del temps de sinterització.

Respecte a la part experimental, s'han fet experiments de sinterització convencional i de *flash sintering* de $BaTiO_3$ comercial. Malauradament no s'ha pogut fer la caracterització de les ceràmiques obtingudes a causa de la pandèmia. S'ha iniciat l'estudi de la sinterització del $Nd_2Zr_2O_7$. De les mostres resultat de la sinterització convencional s'ha determinat la densitat i s'han caracteritzat per difracció de raigs X. S'ha realitzat també espectroscòpia d'impedàncies però no es presenten els resultats, ja que no es disposa del conjunt complet de les mesures que permeti l'anàlisi global.

Paraules clau: *flash sintering*, materials ceràmics, piroclor, difracció de raigs X.

3. INTRODUCTION

Dense ceramic bodies are traditionally produced by sintering green powder compacted at high temperatures and can take several hours. Electric field-assisted sintering (flash sintering) is a new sintering technique that allows to obtain high-density polycrystalline materials at processing times and temperatures dramatically lower than the conventional method, thus reducing energetical and environmental costs. There are a number of variables associated with this technique, such as current and electric field, temperature, processing time, and more. Monitoring these variables during processing allow a thorough control over the microstructure, densification and, as a consequence, an improvement in the functional properties of sintered materials is observed.

The purpose of this work is to study the flash sintering process since flash sintering is at a very early stage, and it seems very promising for the production of materials in an environmentally friendly way with improved properties, hence, improving their applications.

4. OBJECTIVES

The main objective of this essay is to study a ceramic densification method called flash sintering and to explore its application in $Nd_2Zr_2O_7$ sintering, which is an anionic conductor interesting for solid oxide fuel cells (SOFC) applications.

To achieve this purpose, the following points must be fulfilled:

- A bibliographic search to acquire a thorough knowledge about flash sintering characteristics and its possibilities.

- An experimental part. Firstly, flash sintering methodology must be learnt by sintering a commercial compound ($BaTiO_3$) so then, $Nd_2Zr_2O_7$ densification can be carried out. $Nd_2Zr_2O_7$ is previously prepared in 'Química de l'Estat Sòlid' (QES) group.

5. BIBLIOGRAPHIC SEARCH

5.1. METHODS

A bibliographic search was performed from April to June in different data bases, such as SciFinder, Reaxys and Web of Science.

The followed criteria was firstly based on flash sintering advantages over conventional sintering, which developed into a large list of studied materials. Then, flash sintering process was understood by its electrical response, mechanisms, stages and controlling parameters. Additional information about prediction models and experimental setups was found during the searching.

5.2. SINTERING

In order to study materials' electrical properties, highly dense ceramics must be obtained. Powder densification occurs by a combination of a powder-pressing operation and a heating operation in which the formed piece shrinks and experiences a reduction of porosity and an improvement in mechanical integrity. As seen in Fig. 1, these changes occur by the coalescence of the powder particles into a denser mass in a process termed sintering. [1]
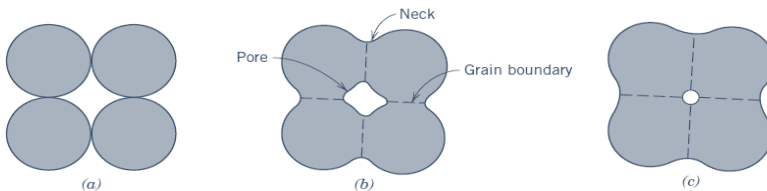
Figure 1. For a powder compact, microstructural changes that occur during heating. (a) Powder particles after pressing. (b) Particle coalescence and pore formation during first sintering moments. (c) As sintering continues, the pores change size and shape.

Sintering phenomenon is due to a solid-state diffusion, which transports grain boundaries matter to the neighbouring grain pores. Currently, it is been mostly performed in a furnace requiring temperatures up to 1500 ºC and many hours. Moreover, it is always accompanied by a

grain growth which slows the sintering process and a possible modification of initial stoichiometry which is caused by the loss of volatile compounds. [2]

5.2.1. Sintering methods (I): pressure-assisted sintering

Pressure-assisted sintering techniques have been developed to optimize properties of sintered materials. Temperature and pressure are the traditional means to refine the microstructures of densified ceramics.

5.2.1.1. Hot pressing (HP)

Hot pressing is the synchronous utilization of uniaxial pressure and heat. Due to uniaxial nature of the procedure, just basic shapes are made by this technique. Further, the application is much more typical in ceramic processing, maybe due the more substantial variety of processing options open to metals or due to particular applications, for example, transparent polycrystalline ceramics, that need fine grain size and high density. [3]

Rangasamy [4] and Sharafi [5] found an application of this technique by densifying $Li_7La_3Zr_2O_{12}$, which is a polycrystalline material used as an electrolyte. The previously mentioned technique produced a highly dense material with a relatively low sintering time.

5.2.1.2. Hot isostatic pressing (HIP)

Hot isostatic pressing simultaneously applies hydrostatic pressure and heat in order to densify a powder sample. The process is comparable to cold isostatic pressing, although elevated temperature and an inert gas transmitting the pressure to the green part are required. Sample powder is generally densified in a container, which operates as a deformable barrier between the green part and the transmitting gas. [3]

5.2.2. Sintering methods (II): electric current assisted sintering

More recently though, field-assisted sintering techniques use electrical fields in combination with previously used temperature and time have been shown to enhance sintering rate. Spark plasma sintering (SPS) and flash sintering (FS) are the more widespread techniques. [6]

5.2.2.1. Spark plasma sintering (SPS)

Spark plasma sintering (SPS) is also known as plasma activated sintering, pulse discharge pressure sintering and pulse electric current sintering. Sintering by this technique is performed

by submitting the green sample to arc discharge generated by a pulsed electric current. An electric discharge phenomenon on a microscopic level promotes material diffusion. The heating rate of SPS is 100-1000 °C/min and the applied pressure is usually 30-200 MPa. [7]

5.2.2.1. Flash sintering (FS)

Flash sintering is an electrical current assisted sintering technique. It has been seen that over an applied field threshold value, sintering might be performed at relatively low temperatures in a few seconds (flash). A great amount of energy and time is saved due to inferior sintering temperatures, obtained when an electric field is applied. This important enhancing phenomenon may be explained as a consequence of Joule effect in grain boundaries where diffusion is promoted, and grain growth is retrained.

Flash sintering studies are in a very early stages as it is a very novel technique. Ceramics, polymers and metals are some of the materials which are being investigated. This technique allows to sinter complex composition materials, it is relevant when working with low melting temperature or low volatility temperature oxides. In addition, nanostructured high-density specimens can be obtained as flash sintering avoids abnormal grain growth. [2]

5.3. FLASH SINTERING

5.3.1. Experimental setup

Flash sintering setup consists of various components. A tubular furnace is responsible for heating up the sample to onset temperatures for flash sintering. The connection between the sample and the power source is made with Pt wires and a Pt paste spread over part of the sample, which will conduct current throughout it. A computer allows to control electrical parameters that a power source supplies and allows to process images captured by a camera. These images display the sample shrinkage during the flash event due to sample's densification, which can be analyzed posteriorly. Optical filters or lenses are required between to furnace and the camera by means of focusing the recording image. Conventional flash sintering setup can be seen in Fig. 2.
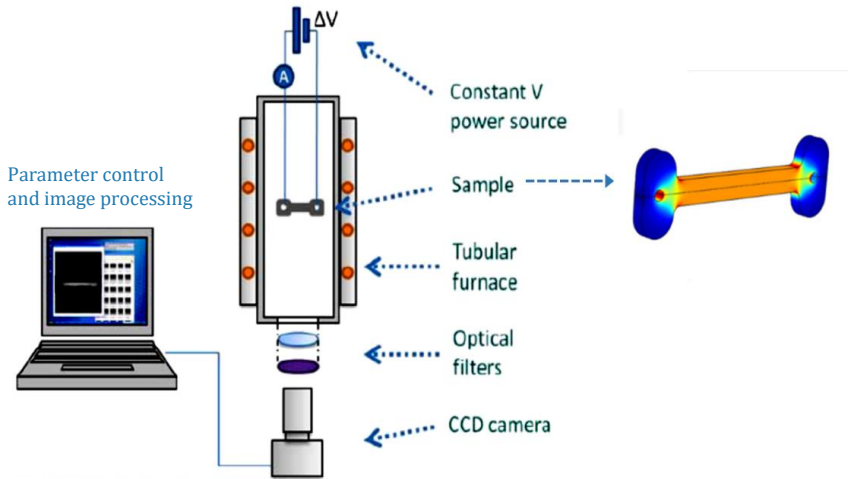
Figure 2. Field-assisted sintering apparatus. Adapted from [8]

More sophisticated setups have been created. In Fig. 3, flash sintering apparatus is coupled together with a dilatometer so shrinkage versus temperature plots are obtained. Consequently, a camera and optical filters are unneeded. Furthermore, the furnace is coupled to an impedance analyser, so impedance spectroscopy data is collected. A power supply is present as in a conventional flash sintering apparatus.

Figure 3. Sketch of the experimental setup for dilatometric measurements, application of voltage and impedance spectroscopy data collection of green ceramic pellets. [9]

5.3.2. Electrical response

At the first part of flash sintering, a constant electric field (V/cm) is applied to the sample while temperature increases. No current passes throughout the sample as it is non-conductive at low temperatures. As temperature keeps rising, necking between the grain occurs and it creates conduction paths for a small current which result in a slight shrinkage of the sample.
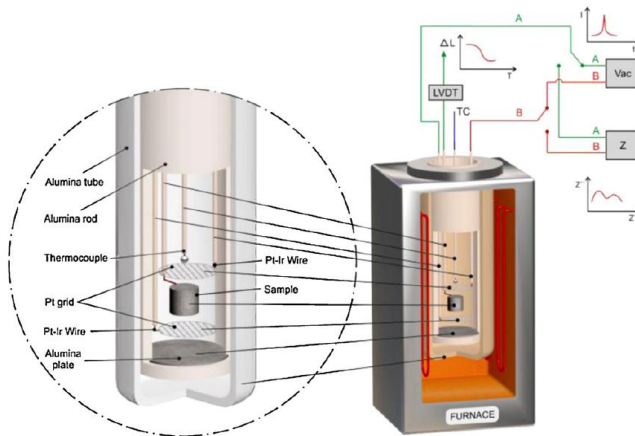
As sample shrinks, apparent electric field increases, and along with increased conductivity due to densification and heating, an exponential rise in current is produced. The abrupt current increase provokes a power dissipation while a constant voltage is applied. At that instant, most of the densification occurs together with pore closure. The sudden current increase needs a pre-set current limit to prevent thermal runaway, hence, the power supply switches from voltage control to current control, which causes steady voltage to decline in order to maintain a constant current. Besides, the power dissipation decreases and approaches a steady state. Plots for power, applied field and intensity during flash sintering process can be seen in Fig. 4a, 4b and 4c respectively. [10] [11]
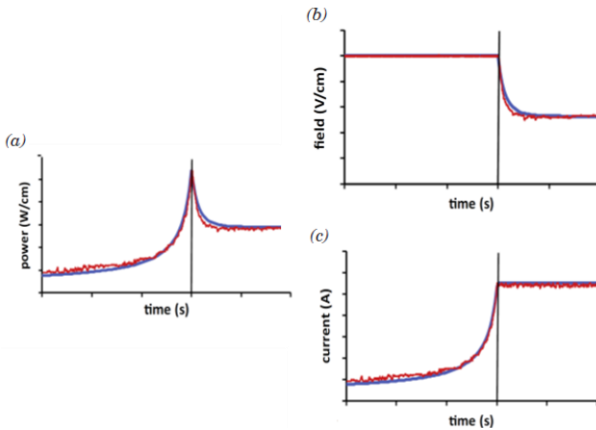
Figure 4. a) Power (W/cm) during flash sintering process, b) Applied field (V/cm) during flash sintering process, c) Current intensity (A) during flash sintering process.

5.3.3. Mechanisms

There is an extensive debate in which is the prevalent mechanism in flash sintering process, a few mechanisms regarding this topic have been discussed: Joule heating, nucleation of Frenkel pairs and electrochemical reactions due to applied voltage.

Joule heating

Electrical current through the specimen can produce Joule heating resulting in a temperature in the specimen that is above the furnace temperature. The higher temperature will enhance the rate of grain boundary diffusion. The flash event is thus recognized to be an effect of runaway Joule heating under voltage control produced by the rapid reduction of resistivity while increasing sample temperature. [12] [13]

Joule heating of the specimen is a mechanism which explains a simultaneous increase in electrical conductivity and mass transport kinetics. [11]

Nucleation of Frenkel pairs

A defect avalanche in the form of Frenkel pairs is precipitated into charge neutral defects and electron-hole pairs. The defects enhance diffusion while the electron-hole pairs induce high conductivity and photoemission. Nucleation is a precursor to the flash onset, and therefore, takes place at the furnace temperature. [14]

Electrochemical reduction due to applied voltage

When working with fuels cells, the applied voltage should not surpass the electrochemical reduction potential. If it does, the ionic conductivity declines while the electronic one increases. The transition from ionic to electronic conductor occurring in flash sintering can also be seen as an effect caused by the electrochemical reduction.

In direct current mode, ionic conductors or mixed ionic conductors follow this sequence of events: (i) the electrochemical reduction initiates from the cathode to the anode, where a significant amount of oxygen ions are released at the anode; (ii) due to the increase of oxygen ions, the conductivity of the sample increases progressively while the electrochemical reduction progresses; (iii) when the material becomes sufficiently conductive for flash sintering and its conductivity becomes essentially electronic a flash event occurs. [6]

5.3.4. Stages

Flash sintering process involves three fundamental stages (Fig. 5) when a constant electric field is applied:

Stage I: incubation

Under a constant electric field, the current density (j) remains low, with a moderate evolution for a lead time (Δt) before the flash event. This current value remains low compared to the current densities reached during flash onset but, significantly greater that the initial current values. Incubation stage is explained by Joule heating and the formation of oxygen vacancies in oxides.

Stage II: flash current increase

After this incubation time, the current density (j) suddenly increments. The onset of the sample densification is coordinated with the abrupt current density increase. Over this momentary period, the large current upsurge results in a power spike, which would cause to a device breakdown and sample damage. The sharp increase results from the migration of oxygen vacancies in oxides to form different charged defects that have an electrostatic interaction between them.

Stage III: current limited stage

When a predefined current density (Imax), is reached, the power supply is therefore either switched from voltage to current control, so that the current density is kept steady during a predefined period or switched down to zero. It is worth noting that densification can progress during a brief period, even after the field is cut off. [15] [16]
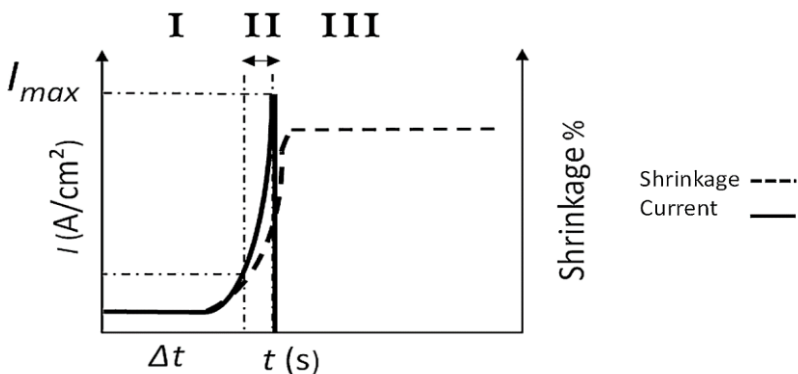

Figure 5. Schematic view of the evolution of current density and shrinkage during the three stages of flash sintering where an electric field is applied at t=0 and the temperature is constant. Adapted from [15]

5.3.5. Parameters adjustment

A variety of factors control flash sintering stages and must be taken into consideration depending on the electrical parameters, bulk properties of the sample and effect of the atmosphere.

The appropriate choice of electric parameters such as applied electric field and current density are important for the event of a flash across the sample to be sintered. Bulk properties of the sample include parameters like the initial particle size, green density and the increase of sample's initial conductivity and their importance is based on the capacity of the electrical power to be delivered to the sample as well on the available route for the electrical current throughout the sample. The atmosphere in which the sample is experimenting flash sintering is also a factor which is determining during flash sintering process.

All the above-mentioned parameters must be controlled in order to achieve a successful sintering. [9]

Applied electric field

Soleimany et al. [17] reported that increasing applied electric fields lead to a nearly constant linear shrinkage for low applied electric field values at a constant current density. However, an increase in the electric field when already at high enough values provokes a tremendous decrease in linear shrinkage which is a measure of enhanced densification.

Shrinkage strain-temperature plots are clear indicators of the difference between flash sintering and field assisted sintering. These plots show two different behaviours depending on the electric field applied. At low applied electric fields, shrinkage strain occurs gradually as temperature is increased while, at higher applied fields, shrinkage strain occurs at a constant temperature. Therefore, at lower applied fields, the sintering rate enhances gradually with applied field resembling field-assisted sintering while above higher fields, sintering occurs in a few seconds which is characteristic of flash sintering. [18]

Effect of current density

Soleimany et al. [17] observed that a current density increase leads to an increase of the specimen temperature because the power increase, so the dissipation of power in form of heat is greater. Moreover, current density has a more pronounced effect on microstructure that voltage has.

Initial particle size

Francis et al. [19] reported that smaller sizes of the initial particles result in a lower temperature for the onset of flash sintering and in a higher densification.

Green density

Du et al. [20] observed that the onset temperature of flash sintering is reduced by increasing green specimens' initial density (powder density) because of higher current densities, resulting in increased Joule heating and faster densification. This agrees with a previous study by Todd et al. [13] who reported that by increasing green specimens' initial density, the applied field required to produce the flash onset was reduced for a given temperature.

Addition of sintering aids

Cologna et al. [8] observed that doping does not influence on sintering kinetics at low fields. However, at high fields, the doped material exhibited flash sintering. One possibility that explains this effect is that the dopant creates local amplifications in the electrical fields which enhance the probability for the nucleation of Frenkel pairs hence, increasing conductivity.

Muccillo et al. [21] evidenced the enhancement of densification by introducing carbon nanotubes (CNTs) in addition to the enhancement due to the application of an electric field. This phenomenon might be explained by a pulse current generation in the presence of CNTs when the applied voltage oscillates. CNTs intermittently react with oxygen, resulting in a carbon dioxide release.

Shomrat et al. [22] observed that flash sintering onset temperatures are determined by the resistance-temperature relation in the sample. Apart from depending on the applied field, it was seen that by enhancing dopant concentration in an oxide sample leads to a conductivity and oxygen vacancy concentrations increase. Onset temperature reduction is proposed as the result of oxygen vacancy concentrations increase since a significant modification of grain size or shape was not observed.

Effect of atmosphere

The dependence of the onset temperature on the atmosphere can be explained by means of increased specimens' initial conductivity in reducing atmospheres. [23]

5.3.6. Prediction of sample temperature from furnace temperature

Flash sintering onset temperature is given by furnace temperature. Although sample temperature is the same as furnace temperature when no current passes through the sample, after current passes through, sample experiments an increment in temperature due to Joule heating.

On one hand, Cologna et al. [2] proposed black-body radiation as a model to estimate temperature differences between the furnace and the sample by assuming that the difference in black-body radiation are equivalent to the heat dissipated by the sample. This assumption can only be considered if the specimen is a monolithic body, meaning that it has a uniform heating. Moreover, losses by conduction and convection are assumed to be negligible due to the fact that black-body radiation is predominant over convection losses at high temperatures, and conduction losses cannot be evaluated normally. The estimation leads to Eq. 1.

$$T_1 = \left[T_0^4 + \frac{W}{A\sigma} \right]^{1/4} \tag{1}$$

Where T_1 stands for the sample temperature; T_0 is then furnace temperature, which is equal to the samples temperature before heating electrically; A is sample's total surface area; W is Joule dissipation of electrical energy and σ which stands for the Stefan-Boltzmann constant ($5.67 \cdot 10^{-8}$ W·m^2/K^4). Eq. 1 assumes the emissivity of the ceramic to be 1; indeed, for most oxides its value is >0.9. Later, the discrepancy between theory and experiment is tied to this assumption: a true emissivity that is less than one would give higher specimen temperatures than calculated. [11]

On the other hand, other researchers have pursued to fully understand and model the relation between furnace temperature and sample temperature since Cologna et al. [2] explained this phenomenon by means of black-body radiation.

Schmerbauch et al. [24] fitted a linear function to predict sample temperature during its heating and while current is flowing through. Their work led to an equation which is used to calculate specimen temperature, which depends on furnace temperature, two thermal expansion coefficients which are specific for each specimen, specimen length when current

passes through the sample and the sample is heating, and specimen length when the sample is non-conductive. Eq. 2 describe the previously mentioned prediction.

$$T_1 = -\frac{n}{m} + \sqrt{\left(\frac{n}{m}\right)^2 + T_0^2 + \frac{2n}{m}T_0 - \frac{2\ln\left(\frac{L(T_0)}{L(T)}\right)}{m}} \tag{2}$$

Where T_1 stands for the sample temperature; T_0 is then furnace temperature, which is equal to the samples temperature before heating electrically; $L(T_0)$ is sample length before switching on the current; $L(T)$ is the sample length after flash sintering; and n and m are coefficients related to thermal expansion, both are specific of each compound.

Temperature difference between furnace and sample may increase moderately in field-assisted sintering techniques (FAST) while in flash sintering, temperature increment is more abrupt for instance reaching differences up to 1000 °C. Moreover, it was observed that current density and specimen temperature follow a linear relationship at various electric fields.

5.3.7. T_onset prediction model

A prediction model to calculate onset temperature for flash sintering at a determined applied field was developed by Dong et al. [25] [26] in order to minimize the experiments needed to reach adequate experimental conditions for each specimen. The prediction model is based on Joule heating mechanism.

As predicted with their analysis, the inverse of onset temperature data $(1/T_{on})$ follow a linear dependence with the Napierian logarithm of the squared applied field $[\ln(E^2/T_{on}^4)]$ at a constant voltage and a constant heating rate as seen in Eq. 3.

$$\ln\left(\frac{E^2}{T_{on}^4}\right) = \frac{E_a}{k_B T_{on}} + \ln\left(\frac{\varepsilon \sigma S d^2 R_0}{\beta}\right) \tag{3}$$

Where T_{on} is the onset temperature, E is the applied field, E_a is the activation energy, k_B is the Boltzmann's constant, ε is the emissivity, σ is the Stefan-Boltzmann constant, S is sample's surface area, d is sample's length, R_0 is a preexponential factor for resistance, β is a numerical constant.

5.3.8. Grain size resulting from flash sintering

Flash sintering technique enhances densification of the sample, and at the same time inhibits grain growth by reason of the current flash passing through the ceramic sample in a short period of time. [9]

Francis et al. [19] reported that smaller grains than in conventionally sintered samples are formed in flash sintering after the flash onset. An explanation for this phenomenon might be a dash of mass into the pores which result in the formation of new smaller grains by nucleation. Half of the mass forming the grains moves during flash sintering when the onset occurs. The brevity of the onset prevents crystal growth and forces the flow of matter to create new grains, hence increasing the densification of the sample. Contrarily, in conventional sintering the process, since the process takes longer periods of time, the inflow of mass that is accumulating on the pore surfaces can be implanted on the crystal surfaces leading to crystal growth rather than creating new smaller grains.

Karakuscu et al. [27] outlined that the average grain size for flash sintered specimens is small and has a narrow grain size distribution, accompanied by a minor far-flung population of larger grains. However, in conventionally sintered specimens, a wider grain size range is observed. Besides, average size is larger as a result of longer sintering times and higher temperatures. Their work led to the conclusion that flash sintering prevents abnormal grain growth, which is more frequently observed in conventionally sintered specimens. Abnormal grain growth prevention with flash sintering technique allows to enhance the sintering process compared to the conventional sintering technique in which grain growth slows the process.

5.3.9. Stoichiometry variations due to volatile compounds losses

Compounds with a complicated synthesis are preferably prepared by the novel method due to the fact that flash sintering operates at lower temperatures which helps to prevent the volatilization of low volatile oxide compounds or melting of low melting temperature specimens.

Shomrat et al. [28] remarked one of the advantages of the flash sintering technique over conventional sintering with regard to potassium niobate ceramics ($KNbO_3$). In $KNbO_3$ synthesis, the problem arises from potassium oxide (K_2O) volatilization above 800 °C which does not maintain stable the stoichiometry of $KNbO_3$. Flückiger et al. [29] evidenced that the weight loss of sample due to K_2O evaporation is increased gradually with temperature.

Contrasted to other ceramic powders which can be fully sintered using the conventional method, applying flash sintering on this compound reduces the volatility of potassium oxide resulting in a high density ceramic due to a rapid sintering process and also resulting in a stoichiometric ratio of K/Nb that remains constant during the whole process. [28]

5.3.10. Flash sintering effects

Materials with new properties are developed by controlling grain size, stoichiometry and by achieving high density samples. These properties must be studied in order to shed a light on flash sintering advantages.

Regarding electrical properties, they might be improved as a result of flash sintering process. In order to characterize samples, impedance spectroscopy is performed. The impedance spectroscopy technique is considered for the analysis of the electrical behaviour of ceramics and has absolute importance in the evaluation of the bulk and interfaces (mainly grain boundaries) electrical resistivities. [9]

Clemenceau et al. [30] observed that the lithium-ion conductivity measured with impedance spectroscopy was 0.5 mS $\cdot$ cm^{-1} at room temperature, and the activation energy was 0.35 eV, similar to the values reported in the literature with conventional or hot-pressing techniques. For similar conductivities, flash sintering was performed at 850 °C in a few seconds, while Murugan et al. [31] densified the same specimen at 1230 °C in 36 hours by conventional sintering. Therefore, flash sintering supposes an advantage when compared to conventional sintering as densification can be achieved at lower temperatures much faster.

Sun et al. [32] noted that the conductivity of $La_{0.8}Sr_{0.2}Ga_{0.8}Mg_{0.2}O_{3-\delta}$ (LGSM) samples sintered at 0.9 A are 0.049 $\sigma \cdot$ cm^{-1} at 800 °C, which is comparable to the value of conventional sintered LSGM samples at 1370 °C in 36 hours by Huang et al. [33]. Once again, flash sintering will save energy and time in the sintering of this compound, and the similar electric properties will be obtained.

Gil-González et al. [34] synthesized phase-pure $BiFeO_3$ by reaction flash sintering of Bi_2O_3 and Fe_2O_3 powders in a few seconds at 625 °C. Sintering is performed jointly with the reaction. Contrarily, Jeon et al. [35] prepared and sintered the compound in two separate stages. Preparation was performed mixing powders by ball milling and posterior calcination. Sintering at 800 °C for 12 hours, which allowed to reach high densities. Therefore, flash sintering not only

proved to be an efficient technique for achieving improved densifications in a short time, but also showed that can avoid extended sample preparations through contributing to the reaction.

A comparative table between conventional and flash sintering conditions can be seen in Appendix 1, in which lower onset temperatures and shorter dwell times for flash sintering than in conventional sintering are displayed.

6. EXPERIMENTAL PART

6.1. INTRODUCTION

6.1.1. Pyrochlore structure

Pyrochlore structure is named after the mineral pyrochlore which has the approximate composition $(CaNa)Nb_2O_6F$. Pyrochlore compounds represent an isostructural phase family to the mineral pyrochlore. [36] Concerning applications, pyrochlore structured materials are used in methane reforming [37], photocatalysis [38], photoluminescence [39], dielectric materials [40][41], magnetic materials [42][43], giant magnetoresistances [44][45] and superconductors [46][47].

Pyrochlore compounds' general formula is $A_2B_2O_6O'$ with four crystallographically non-equivalent kinds of atom [48], where A is a divalent or trivalent large cation with an octahedral coordination (e.g.: lanthanides) and B is typically a pentavalent or tetravalent high-field transition metal with an hexagonal coordination, respectively (e.g.: Zr, Nb, Ti) [49]. Its structure derives from a fluorite-type structure (CaF_2), nevertheless the cationic sub-lattice is well-organized and there is an anion vacancy in an eighth of the total number of tetrahedral holes. Pyrochlore structure shown in Fig. 6, belongs to a space group Fd-3m and it contains eight formula units for each unit cell (Z=8) [50]. Fig. 7 exhibits an eighth of a pyrochlore unit cell.

The structure may be described as an A_2O framework interpenetrating the B_2O_6 octahedral framework which is justified by the appreciable distances between A-6O and A-2O in the coordination group around A. [36]

Regarding Wyckoff positions, A^{3+} cations are located at 16d site while B^{4+} cations are located at 16c site. Two types of oxygen anions (O^{2-}) are found in 48f and 8b sites. The inherent oxygen vacancy in 8a site is responsible for the high mobility of oxide anions, thus creating a mechanism to modulate conductivity through the defects' concentration in the pyrochlore structure. [50]

Electrical properties in pyrochlore-type oxide-ion conductors are related to the degree of structural disorder which is governed by the ionic radius ratio (R_A/R_B). For an ionic radius ratio below 1.46, the disorder in the ionic sub-lattices is complete and this might render a fluorite-type defect structure. For ionic radius above 1.78 laminar perovskites are rendered. Pyrochlore structure is obtained for ionic radius values ranging from 1.46 to 1.78. [51]
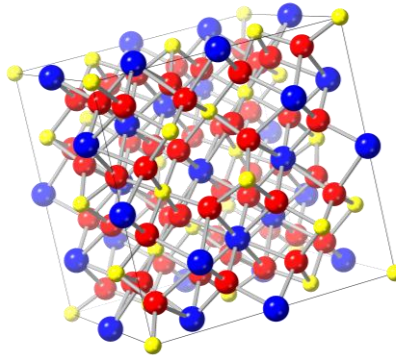

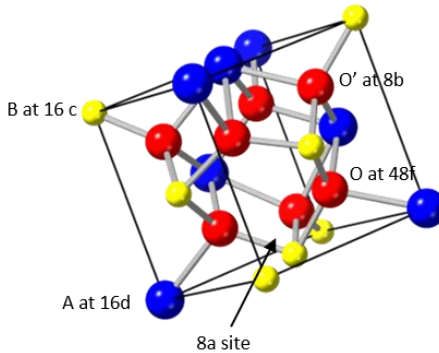Figure 6. Pyrochlore structure. [153227-ICSD]

Figure 7. Partial unit cell of pyrochlore (Fd-3m), blue spheres represent A^{3+} cations, yellow spheres B^{4+} cations and red spheres O^{2-} anions, the arrow indicates an additional ionic vacancy. [153227-ICSD]

6.1.2. ZrO$_2$-Nd$_2$O$_3$ phase diagram

The ZrO$_2$–Nd$_2$O$_3$ binary system phase diagram acquired using high temperature X-ray analysis [52] is shown in Fig. 8. The fluorite-type structure (F) is stabilized at a low-temperature range by adding Neodymium (Nd). Nevertheless, the increase of neodymium oxide (Nd$_2$O$_3$) composition in the mixture leads to the appearance of the pyrochlore structure (Pyr).

The red line in the phase diagram (Fig. 8) indicates the region where a single pyrochlore phase with a specific Nd$_2$Zr$_2$O$_7$ composition is constituted. Consequently, it is laborious to obtain the pyrochlore phase without secondary phases.
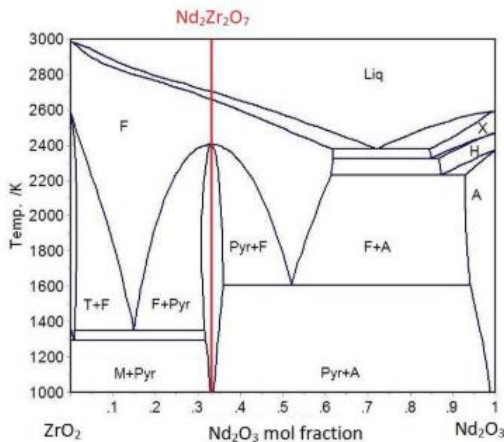
Figure 8. Phase diagram of ZrO$_2$–Nd$_2$O$_3$ binary system where M = monoclinic, T= tetragonal, F= fluorite, Pyr = pyrochlore, A= hexagonal at low temperature, H= hexagonal at high temperature, X= cubic.

6.1.3. X-ray diffraction (XRD)

XRD diffraction is a technique used to characterize different crystalline materials. This technique is based on the scattering of X-ray beams. X-rays are electromagnetic radiation that are originated when high-energy charged particles, e.g. electrons, collide with matter. Regarding Cu lamp, incident electrons have the enough energy to ionize Cu 1s electrons. Hence, an electron of 2p or 3p levels instantly drops down to occupy the vacant 1s level as it shown in Fig. 9a. The energy released in the transition produces X-rays.

Fig. 9. a) Cu emission spectrum. b**)** Generation of Cu K_α X-rays

There are different fixed values of transitions energies. In the case of Cu, the 2p to 1s transition is called K_α, which has a wavelength of 1.5418 Å. Transition from 3p to 1s is called K_β, which has a wavelength of 1.3922 Å. K_α transition occurs more frequently than K_β transition. Ind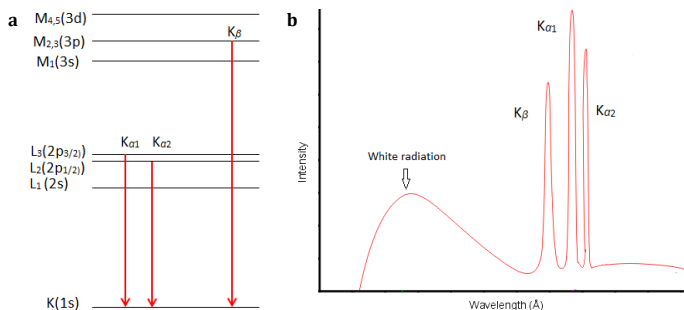eed, the K_α radiation is a doublet (Fig. 9b) that occurs for the two possible spin states ($K_{\alpha 1}$ = 1.54051 Å and $K_{\alpha 2}$ =1.54433 Å) of the 2p level.

In diffraction experiments that use a Cu lamp, the K_α line is the most energetic and it is desired to filter out all other wavelengths. A sheet of Ni foil is an adequate filter, as the required energy to ionize a 1s electron of Ni corresponds to a wavelength of 1.488 Å, which is in the middle of K_α and K_β line wavelengths in Cu emission spectrum. Therefore, K_β is energetically able to ionize 1s electron of Ni while K_α is not able to ionize it. [53]

X-ray beams are diffracted in many directions when colliding with the sample. Bragg's law allows to analyze these beams. This law can be explained with two X-ray beams (Fig.10), A and B, which are reflected in a plane with an angle equal to incidence angle and one of these beams must travel an extra distance. Besides, Bragg's law gives the conditions for X-ray beams constructive interferences. Then, if Bragg's law is satisfied, reflected beams are in phase and interfere constructively. Contrarily, at incidence angles other than Bragg angle, reflected beams are out-of-phase and result in a destructive interference or cancellation. This phenomenon is described by Bragg's law: $2\,d\sin\theta = n\,\lambda$, where d is the interplanar distance, λ is the incident wavelength, n is a whole number (usually n=1) and θ is the angle.
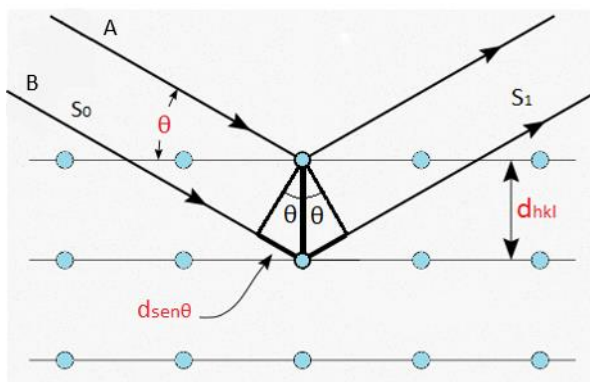
Figure 10. Representation of Bragg's law.

The X-ray powder diffraction pattern is shown by a set of lines or peaks, each of different position (d-spacing or Bragg angle, θ) and intensity. Line positions in the diffraction pattern are fixed and characteristic for each substance. The intensities can subtly vary for a determined substance depending on the preparation method and instrumental conditions. Crystal's symmetry is explained by the number of peaks present in the sample, thus a lot of peaks imply low symmetry. Phase determination and crystallographic planes determination is possible with XRD due to the fact that each plane has different Miller indexes (hkl). Hence, the determination is achieved by comparing the results with reference diffraction patterns from The International Centre for Diffraction Data (ICCD). Unit cell parameters (a, b, c, α, β and γ) can be calculated once the crystallographic planes have been designated.

XRD studies were carried out with PAnalytical X'Pert PRO MPD diffractometer. K_α line of Cu (1.5404 Å) was used at 30 mA and 40 kV. The diffraction pattern was recorded for 2θ angles from 10º to 100º and the scanning speed was 1 ºC/min. X'Pert HighScore Plus software was used to interpret the diffraction patterns.

6.2. BaTiO$_3$ CONVENTIONAL AND FLASH SINTERING

Conventional sintering and flash sintering of a commercial BaTiO$_3$ sample (Merck Ref. 12048) was performed. Sample preparation for the sintering process consisted on mixing commercial BaTiO$_3$ with 6 wt.% PVA and molding the mixture into a dog-bone shape by applying a uniaxial pressure of 270 MPa, generated by a hydraulic press. The dies used for molding and the dog-bone-shape can be seen in Fig. 11 and Fig. 12, respectively.

Figure 11. Picture of the dies used for molding the samples into a dog-bone shape with the application of a uniaxial pressure.
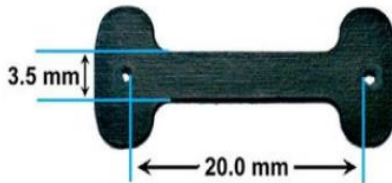
Figure 12. Picture of the dog-bone shape and dimensions.

6.2.1. BaTiO$_3$ conventional sintering

Sample preparation in conventional sintering is followed by the introduction of the dog-bone shaped sample into a furnace where a temperature program is applied as seen in Fig. 13. Heating up the sample to high temperatures during a large period of allowed its densification.
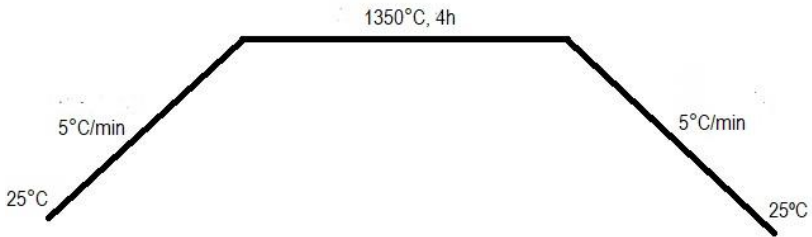
Figure 13. Scheme of the temperature program for conventionally sintered $BaTiO_3$.

Sintered relative densities were not calculated. Neither do characterization methods were performed due to the pandemic.

6.2.2. BaTiO₃ flash sintering

Sample preparation in flash sintering is followed by the introduction of the dog-bone shaped sample into a furnace where a temperature program is applied as seen in Fig. 14. The first temperature program is intended to pre-sinter the sample and remove the binder (PVA) added during sample preparation.

Pre-sintered sample's density of $BaTiO_3$ was measured to be 3.00 g/cm^3 and theoretical density of $BaTiO_3$ is 6.01 g/cm^3 so green density of the sample is 49.9 %.
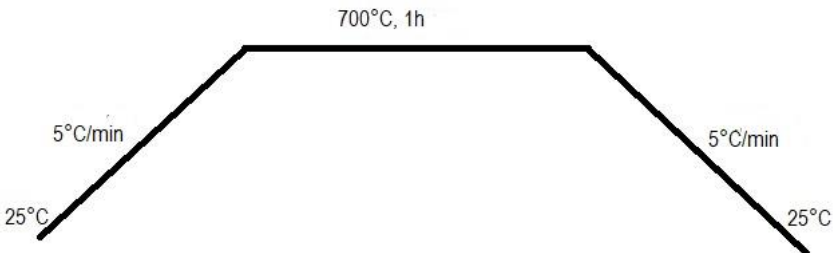
Figure 14. Scheme of the temperature program for pre-sintering $BaTiO_3$.

Afterwards, the dog-bone sample was partially painted with a paste of Pt in order to become electrically conductive and it was attached to the tubular furnace by Pt wires as seen in Fig. 15.

Flash sintering setup can be seen in Fig. 16, where the computer controls the voltage, current density and other parameters which are supplied by the power supply, the tubular furnace heats up the sample, and the lenses and the camera record images of the flash event so a further processing can be performed with the computer.
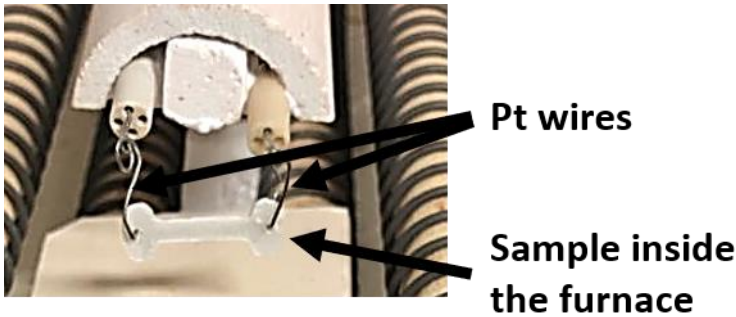
Figure 15. Picture of the dog-bone shape pre-sintered sample attached to the tubular furnace by Pt wires.
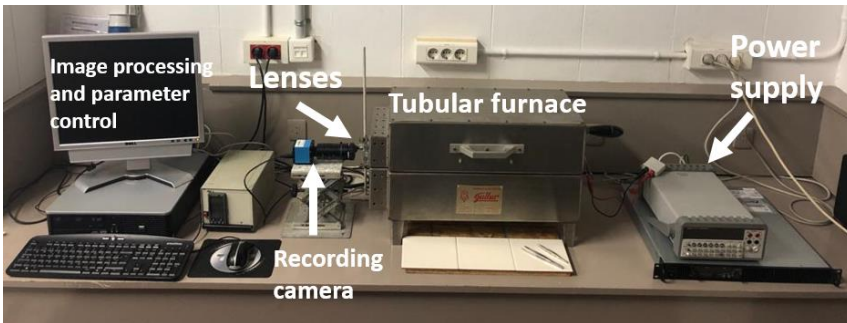
Figure 16. Picture of the setup for the flash sintering process.

Two experiments were performed under different conditions in order to optimize sintering process. In all the experiments, an initial fast temperature ramp was set until 600 °C and then a slower temperature ramp of 10 °C/min was planned until 1200 °C.

The first flash sintering experiment was carried out with a 200 V/cm applied field and a 10 mA/mm^2 current density. Onset temperature of 986 °C was achieved under these conditions. Dwell time was set at 10 min after which the voltage at the current limit was 164 V.

A second experiment was carried out with a 300 V/cm applied field and a 15 mA/mm^2 current density. Onset temperature of 927 °C was achieved under these conditions. Dwell time was set at 10 min after which the voltage at the current limit was 240 V.

Sintered relative densities were not calculated. Neither do characterization methods were performed due to the pandemic.

6.3. Nd$_2$Zr$_2$O$_7$ CONVENTIONAL SINTERING

Conventional sintering of a Nd$_2$Zr$_2$O$_7$ (NZO) product previously synthesized in the Solid-State Chemistry Group (QES) group was performed.

The preparation of three NZO pellets was accomplished by applying a uniaxial of 270 MPa with a hydraulic press followed by a sintering process in a furnace with the temperature program seen in Fig. 17.
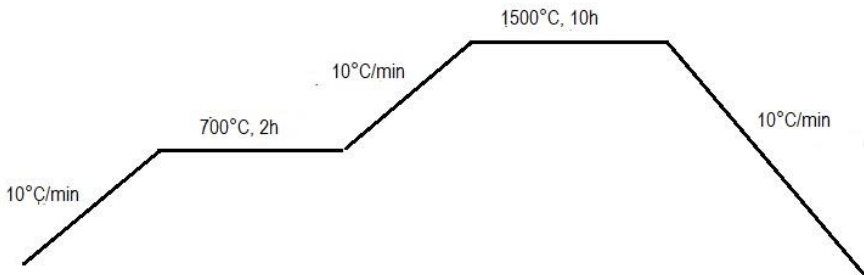
Figure 17. Scheme for the temperature program of conventionally sintered Nd$_2$Zr$_2$O$_7$.

The pellets were labelled depending on subsequent characterizations: X-ray diffraction (XRD), scanning electron microscopy-energy dispersive X-ray spectroscopy (SEM-EDS) and impedance spectroscopy (IS).

6.3.1. X-ray diffraction (XRD) discussion

When comparing NZO diffractometer with an NZO pattern (PDF card: #00-017-0458), even though relative intensity is below 2%, an unusual peak at 2θ=32.5240 ° was visible. This peak was associated to a cubic Nd_2O_3 secondary phase (PDF card: #00-021-0579) as seen in Fig. 18. Secondary phases might be present in the sample as the pyrochlore structure is only obtained at a specific stoichiometry, as seen in phase diagram of the ZrO_2–Nd_2O_3 binary system. A slight variation in ZrO_2 or Nd_2O_3 composition in the mixture will result in a biphasic system. Therefore, pyrochlore structure is difficult to obtain.
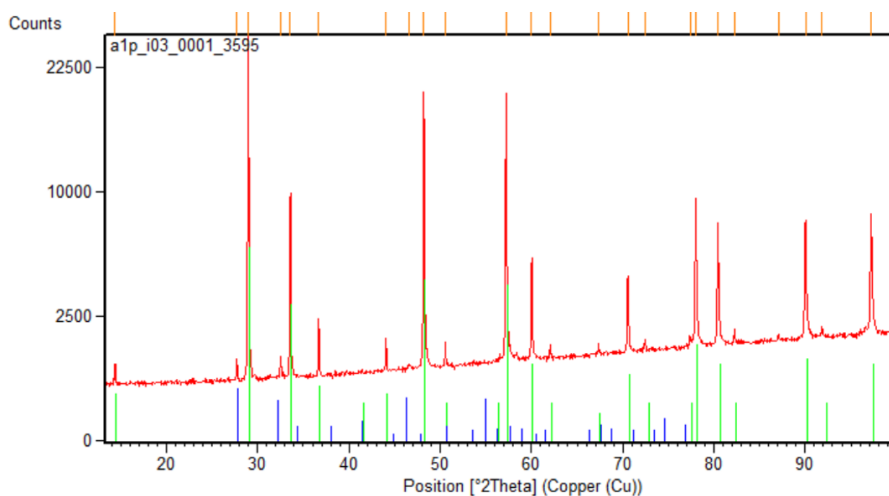
Figure 18. Diffractogram for NZO conventionally sintered. In red, NZO sample; in green, NZO pattern; in blue, cubic Nd_2O_3 pattern.

6.3.2. Density determination

Sample's density was determined based in Archimedes principle and it was performed using a KERN ABJ/ABS analytical balance with the density determination supplementary set as seen in Fig. 19.

Figure 19. Picture of the KERN ABJ/ABS analytical balance with density determination supplementary set.

Sample's density is determined with Eq. 4.

$$\rho = \frac{A}{A - B} \, \rho_o \qquad (4)$$

Where, ρ is the sample's density, A is the sample's mass in air, B is the sample's mass in the measurement liquid and ρ_o is water's density at the working temperature.

Theoretical density of NZO is 6.41 g/cm^3, while sintered sample's density was 6.30 g/cm^3. The resulting sintered relative density was 98.4 %.

6.3.3. Impedance spectroscopy (IS)

IS pellet was covered in gold by sputtering and the edges were smoothened with glass paper in order to obtain two electrodes and a conductive sample. Pellet's dimensions were measured before executing IS measurements. A frequency sweep (0.005-1000 kHz) and temperature sweep (350-800 °C) were performed in IS. The characterization was carried out by impedance spectroscopy with an impedance analyser HP 4192A from the QES group. Results were not analyzed due to the lack of measurements at different atmospheres.

7. CONCLUSIONS

To sum up, the following conclusions are extracted:

Bibliographic research has allowed to retrieve a relevant amount of information about flash sintering basis and working methodology.

- Flash sintering obtained knowledge will facilitate the experimental design and the optimization of experimental conditions for densification.
- Comparative studies of conventional sintering and flash sintering about densified materials' properties have barely been found.

Experimental part has been vastly reduced due to COVID19 impact, although:

- Sample preparation for sintering experiments has been learnt.
- Some experiments have been carried out, which helped to understand the bibliographic information retrieved.

A final conclusion can be highlighted, a thorough knowledge has been acquired about flash sintering technique which will allow to apply it to different materials studied in 'Química de l'Estat Sòlid' (QES) group and will allow to assess how sintering process modifies materials' functional properties.

8. REFERENCES AND NOTES

1. Callister Jr., W. D.; Rethwisch D. G. *Callister's Material Science and Engineering,* 8th ed.; John Wiley & Sons, Inc.: Hoboken, 2010.
2. Cologna, M.; Rashkova, B.; Raj, R. Flash sintering of nanograin zirconia in <5 s at 850 °C. *J. Am. Ceram. Soc.* **2010**, *93 (11)*, 3556-3559.
3. Francis, L. *Materials Processing: A Unified Approach to Processing of Metals, Ceramics and Polymers,* 1st ed.; Elsevier B. V.: Amsterdam, 2015.
4. Rangasamy, E.; Wolfenstine, J.; Sakamoto, J. The role of Al and Li concentration on the formation of cubic garnet solid electrolyte of nominal composition $Li_7La_3Zr_2O_{12}$. *Solid State Ionics.* **2012**, *206*, 28-32.
5. Sharafi, A.; Meyer, H. M.; Nanda, J.; Wolfenstine, J.; Sakamoto, J. Characterizing the Li-$LiLa_7La_3Zr_2O_{12}$ interface stability and kinetics as a function of temperature and current density. *J. Power Sources.* **2016**, *302*, 135-139.
6. Yu, M.; Grasso, S.; Mckinnon, R.; Saunders, T.; Reece, M. J. Review of flash sintering: materials, mechanisms and modelling. *Adv. Appl. Ceram.* **2016**, *116 (1)*, 24-60.
7. Guo, J.; Li J.; Kou H. *Modern Inorganic Synthetic Chemistry,* 1st ed.; Elsevier B. V.: Amsterdam, 2011.
8. Cologna, M.; Francis, J. S. C.; Raj, R. Field assisted and flash sintering of alumina and its relationship to conductivity and MgO-doping. *J. Eur. Ceram. Soc.* **2011**, *31*, 2827-2837.
9. Muccillo, R.; Muccillo, E. N. S. An experimental setup for shrinkage evaluation during electric field-assisted flash sintering: Application to yttria-stabilized zirconia. *J. Eur. Ceram. Soc.* **2013**, *33*, 515-520.
10. Charalambous, H.; Jha, S. K. Inhomogeneous reduction and its relation to grain growth of titania during flash sintering. *Scr. Mater.* **2018**, *155*, 37-40.
11. Raj, R. Joule heating during flash-sintering. *J. Am. Ceram. Soc.* **2012**, *32*, 2293-2301.
12. Raj, R; Cologna, M.; Francis, J. S. C. Influence of externally imposed and internally generated electrical fields on grain growth, diffusional creep, sintering and related phenomena in ceramics. *J. Am. Ceram. Soc.* **2011**, *94 (7)*, 1941-1965.
13. Todd, R. I.; Zapata-Solvas, E.; Bonilla, R. S.; Sneddon, T.; Wilshaw, P. R. Electrical characteristics of flash sintering: thermal runaway of Joule heating. *J. Eur. Ceram. Soc.* **2015**, *35,* 1865-1877.
14. Naik, K. S.; Sglavo, V. M.; Raj R. Flash sintering as a nucleation phenomenon and a model thereof. *J. Eur. Ceram. Soc.* **2014**, *34,* 4063-4067.
15. Bichaud, E.; Chaix, J. M.; Carry, C.; Kleitz, M.; Steil, M. C. Flash sintering incubation in Al_2O_3/TZP composites. *J. Eur. Ceram. Soc.* **2015**, *35,* 2587-2592.
16. Ren, K.; Wang, Q.; Lian, Y.; Wang, Y. Densification kinetics of flash sintered 3 mol% Y_2O_3 stabilized zirconia. *J. Alloys Compd.* **2018**, *747,* 1073-1077.
17. Soleimany, M.; Padyar, M. H. Investigation on flash sintering of $BaZr_{0.1}Ce_{0.7}Y_{0.2}O_{3-\delta}$ compound; using nickel wire as electrode material. *Ceram. Int.* **2020**, *46,* 2128-2138.
18. Prette, A. L. G.; Cologna, M.; Sglavo, V.; Raj, R. Flash-sintering of Co_2MnO_4 spinel for oxide fuel cell applications. *J. Power Sources.* **2011**, 196, 2061-2065.
19. Francis, J. S. C.; Cologna, M.; Raj, R. Particle size effects in flash sintering. *J. Eur. Ceram. Soc.* **2012**, *32,* 3129-3136.
20. Du, Y.; Stevenson, A. J.; Vernat, D.; Diaz, M.; Marinha, D. Estimating Joule heating and ionic conductivity during flash sintering of 8YSZ. *J. Eur. Ceram. Soc.* **2016**, *36, 749-*759.

21. Muccillo, R.; Ferlauto, A. S.; Muccillo, E. N. S. Flash sintering samaria-doped ceria-carbon nanotube composites. *Ceramics.* **2019**, *2*, 64-73.

22. Shomrat, N.; Baltianski, S.; Dor, E.; Tsur, Y. The influence of doping on flash sintering conditions in $SrTi_{1-x}Fe_xO_{3-\delta}$. *J. Eur. Ceram. Soc.* **2017**, *37,* 179-188.

23. Zhang, Y.; Luo, J. Promoting the flash sintering of ZnO in reduced atmospheres to achieve nearly full densities at furnace temperatures of <120 °C. *Scr. Mater.* **2015**, *106*, 26-29.

24. Schmerbauch, C.; Gonzalez-Julian, J.; Röder, R.; Ronning, C.; Guillon, O. Flash sintering of nanocrystalline zinc oxide and its influence on microstructure and defect formation. *J. Am. Ceram. Soc.* **2014**, *97 (6)*, 1728-1735.

25. Dong, Y.; Chen, I. Predicting the onset of flash sintering. *J. Am. Ceram. Soc.* **2015**, *98 (8)*, 2333-2335.

26. Dong, Y.; Chen, I. Onset criterion for flash sintering. *J. Am. Ceram. Soc.* **2015**, *98 (12)*, 3624-3627.

27. Karakuscu, A.; Cologna, M.; Yarotski, D.; Won, J.; Francis, J. S. C.; Raj, R.; Uberuaga, B. P. *J. Am. Ceram. Soc.* **2012**, *95 (8)*, 2531-2536.

28. Shomrat, N.; Baltianski, S.; Randall, C. A.; Tsur, Y. Flash sintering of potassium-niobate. *J. Eur. Ceram. Soc.* **2015**, *35,* 2209-2213.

29. Flückiger, U.; Arend, H. On the preparation of pure, doped and reduced $KNbO_3$ single crystals. *J. Cryst. Growth.* **1978**, *43*, 406-416.

30. Clemenceau, T.; Andriamady, N.; Kumar, P. M. K.; Bardan, A.; Avila, V.; Dahl, K.; Hopkins, M.; Vendrell, X.; Marshall, D.; Raj, R. Flash sintering of Li-ion conducting ceramic in a few seconds at 850 °C. *Scr. Mater.* **2019**, *172*, 1-5.

31. Murugan, R.; Thangadurai, V.; Weppner, W. Fast lithium ion conduction in garnet-type $Li_7La_3Zr_2O_{12}$. *Angew. Chem. Int. Ed.* **2007**, *46*, 7778-7781.

32. Sun, K.; Zhang, J.; Jiang, T; Qiao, J.; Sun, W.; Rooney, W. Flash-sintering and characterization of $La_{0.8}Sr_{0.2}Ga_{0.8}Mg_{0.2}O_{3-\delta}$ electrolytes for solid oxide fuel cells. *Electrochim. Acta.* **2016**, *196*, 487-495.

33. Huang, K.; Feng, M.; Goodenough, J. B. Sol-gel synthesis of a new oxide-ion conductor Sr- and Mg-doped $LaGaO_3$ perovskite. *J. Am. Ceram. Soc.* **1996**, *79 (4)*, 1100-1104.

34. Gil-González, E.; Perejón, A.; Sánchez-Jiménez, P. E.; Sayagués, M. J.; Raj, R.; Pérez-Maqueda, L. A. Phase-pure $BiFeO_3$ produced by reaction flash-sintering of Bi_2O and Fe_2O_3. *J. Mater. Chem. A.* **2018**, *6*, 5356-5366.

35. Jeon, N.; Moon, K.-S.; Rout, D.; Kang, S.-J. L. Enhanced sintering behaviour and electrical properties of single phase $BiFeO_3$ prepared by attrition milling and conventional sintering. *J. Korean Ceram. Soc.* **2012**, *49 (6)*, 485-492.

36. Wells, A. F. Química inorgánica estructural*, 1st ed.; Ed. Reverté: Barcelona, 1978.

37. Kumar, N.; Kanitkar, S.; Wang, Z.; Haynes, D. Dry reforming of methane with isotopic gas mixture over Ni-based pyrochlore catalyst. *Int. J. Hydrogen Energy.* **2019**, *44*, 4167-4176.

38. Uno, M.; Kosuga, A.; Okui, M.; Horisaka, K.; Muta, H.; Kurosaki, K.; Yamanaka, S. Photoelectrochemical study of lanthanide zirconium oxides, $Ln_2Zr_2O_7$ (Ln = La, Ce, Nd and Sm). *J. Alloys Compd.* **2006**, *420,* 291-297.

39. Zhang, A.; Lü, M.; Zhou, G.; Wang, S.; Zhou, Y. Combustion synthesis and photoluminescence of Eu^{3+}, Dy^{3+}-doped $La_2Zr_2O_7$ nanocrystals. *J. Phys. Chem. Solids.* **2006**, *67,* 2430-2434.

40. Rao, P. P.; Liji, S. J.; Nair, K. R.; Koshy, P. New pyrochlore-type oxides in Ca-R-Ti-Nb-O system (R = Y, Sm or Gd)—structure, FT-IR spectra and dielectric properties. *Mater. Lett.* **2004**, *58,* 1924-1927.

41. Paściak, M.; Wołcyrz, M.; Pietraszko, A.; Leoni, S. Local structure in the paraelecric phase of $Cd_2Nb_2O_7$ determined from x-ray diffuse scattering, by means of *ab initio* molecular dynamics and Monte Carlo modeling. *Phys. Rev. B.* **2010**, *81 (1),* 014107/1-014107/6.

42. Chamberlain, S. L.; Hess, S. T.; Corruccini, L. R. Dipolar magnetic order in the pyrochlore structure. *Phys. Lett. A.* **2004**, *323,* 310-314.

43. Raju, N. P.; Dion, M.; Gingras, M. J. P.; Mason, T. E.; Greedan, J. E. Transition to long-range magnetic order in the highly frustrated insulating pyrochlore antiferromagnet $Gd_2Ti_2O_7$. *Phys. Rev. B.* **1999**, *59 (22),* 14489-14498.

44. Shimakawa, Y.; Kubo, Y.; Manako, T. Giant magnetoresistance in $Tl_2Mn_2O_7$ with the pyrochlore structure. *Nature.* **1996**, *379,* 53-55.

45. Hwang, H. Y.; Cheong, S.-W. Low-field magnetoresistance in the pyrochlore $Tl_2Mn_2O_7$. *Nature.* **1997**, *389,* 942-944.

46. Hanawa, M.; Muraoka, Y.; Tayama, T.; Sakakibara, T.; Yamaura, J.; Hiroi, Z. Superconductivity at 1 K in $Cd_2Re_2O_7$. *Phys. Rev. Lett.* **2001**, *87 (18),* 187001/1-187001/4.

47. Yoshimura, K.; Sakai, H.; Ohno, H.; Kambe, S.; Walstedt R. E. Physical properties of new superconductor $Cd_2Re_2O_7$ with the pyrochlore-type structure. *Physica B.* **2003**, *329-333,* 1319-1320.

48. Subramanian, M. A.; Aravamudan, G.; Subba Rao, G. V. Oxide pyrochlores – A review. *Prog. Solid St. Chem.* **1983**, *15,* 55-143.

49. Atencio, D.; Andrade, M. B.; Christy, A. G.; Gieré, R.; Kartashov, P. M. The pyrochlore supergroup of minerals: Nomenclature. *Can. Mineral.* **2010**, *48,* 569-594.

50. Stanek, C. R.; Minervini, L.; Grimes, R. W. Nonstoichiometry in $A_2B_2O_7$ pyrochlores. *J. Am. Ceram. Soc.* **2002**, *85 (11),* 2792-2798.

51. Díaz-Guillén, J. A.; Díaz-Guillén, M. R.; Almanza, J. M.; Fuentes, A. F.; Santamaría, J.; León, C. Effect of La substitution for Gd in the ionic conductivity and oxygen dynamics of fluorite-type $Gd_2Zr_2O_7$. *J. Phys.: Condens. Matter.* **2007**, *19 (35),* 356212.

52. Fabrichnaya, O.; Seifert, H. J. Assessment of thermodynamic functions in the ZrO_2-Nd_2O_3-Al_2O_3 system. *CALPHAD: Comput. Coupling Phase Diagrams Thermochem.* **2008**, *32,* 142-151.

53. West, A. R. *Solid state chemistry and its applications,* 2nd ed.; John Wiley & Sons, Inc.: Hoboken, 2014.

54. Ji, W.; Parker, B.; Falco, S.; Zhang, J. Y.; Fu, J. Y.; Todd, R. I. Ultra-fast firing: Effect of heating rate on sintering of 3YSZ, with and without an electric field. *J. Eur. Ceram. Soc.* **2017**, *37,* 2547-2551.

55. Carvalho, S. G. M.; Muccillo, E. N. S.; Muccillo, R. Electrical behaviour and microstructural features of electric field-assisted and conventionally sintered 3 mol% yttria-stabilized zirconia. *Ceramics.* **2018**, *1,* 3-12.

56. Liu, D.; Li, X.; Liu, F.; Gao, Y.; Ren, K.; Wang, Y. Effect of the current density on the densification of 3 mol% yttria-stabilized zirconia in flash sintering. *J. Alloys Compd.* **2020**, *825,* 154061.

57. M'Peko, J.-C. Flash sintering in well-dispersed insulator-ionic conductor composites: The case of diphasic alumina-zirconia (Al_2O_3-3YSZ) system. *Scr. Mater.* **2020**, *175,* 38-42.

58. Azhar, A. Z. A.; Ratnam, M. M.; Ahmad, Z. A. Effect of Al_2O_3/YSZ microstructures on wear and mechanical properties of cutting inserts. *J. Alloys Compd.* **2009**, *478,* 608-614.

59. Muccillo, R.; Kleitz, M.; Muccillo, E. N. S. Flash grain welding in yttria stabilized zirconia. *J. Eur. Ceram. Soc.* **2011**, *31,* 1517-1521.

60. Downs, J. A.; Sglavo, V. M. Electric field assisted sintering of cubic zirconia at 390 °C. *J. Am. Ceram. Soc.* **2013**, *96 (5),* 1342-1344.

61. Steil, M. C.; Marinha, D.; Aman, Y.; Gomes, J. R. C.; Kleitz, M. From conventional ac flash-sintering to hyper-flash and double flash. *J. Eur. Ceram. Soc.* **2013**, *33,* 2093-2101.

62. Muccillo, R.; Muccillo, E. N. S. Shrinkage control of yttria-stabilized zirconia during ac electric field-assisted sintering. *J. Eur. Ceram. Soc.* **2014**, *34,* 3871-3877.

63. Dahl, P.; Kaus, I.; Zhao, Z.; Johnsson, M.; Nygren, M.; Wiik, K.; Grande, T.; Einarsrud, M.-A. Densification and properties of zirconia prepared by three different sintering techniques. *Ceram. Int.* **2007**, *33,* 1603-1610.

64. Prette, A. L. G.; Cologna, M.; Sglavo, V.; Raj, R. Flash-sintering of Co_2MnO_4 spinel for solid oxide fuel cell applications. *J. Power Sources.* **2011**, *196,* 2061-2065.

65. Prette, A. L. G. (2011). *Sintering of Co_2MnO_4 spinel for protective coatings in SOFC* [PhD thesis, Università Degli Studi Di Trento] https://eprints-phd.biblio.unitn.it/542/

66. Zhao, J.; Harmer, M. P. Sintering of ultra-high-purity alumina doped simultaneously with MgO and FeO. *J. Am. Ceram. Soc.* **1987**, *70 (12)*, 860-866.

67. Biesuz, M.; Sglavo, V. M. Current-induced abnormal and oriented grain growth in corundum upon flash sintering. *Scr. Mater.* **2018**, *150*, 82-86.

68. Pulgarín, H. L. C.; Albano, M. P. Sintering and microstructure of Al_2O_3 and Al_2O_3-ZrO_2 ceramics. *Procedia Mater. Sci.* **2015**, *8*, 180-189.

69. Muccillo, R.; Muccillo, E. N. S; Kleitz, M. Densification and enhancement of grain boundary conductivity of gadolinium-doped barium cerate by ultra fast flash grain welding. *J. Eur. Ceram. Soc.* **2012**, *32,* 2311-2316.

70. Maffei, N.; Pelletier, L.; McFarlan, A. Performance characteristics of Gd-doped barium cerate-based fuel cells. *J. Power Sources.* **2014**, *136*, 24-29.

71. Muccillo, R.; Esposito, V.; de Florio, D. Z.; Muccillo, E. N. S. Electric field-assisted pressureless sintering gadolinium-, yttrium- and samarium-doped barium cerate. *Scr. Mater.* **2018**, *156*, 6-9.

72. Amsif, N.; Marrero-Lopez, D.; Ruiz-Morales, J. C.; Savvin, S. N.; Gabás, M.; Nuñez, P. Influence of rare-earth doping on the microstructure and conductivity of $BaCe_{0.9}Ln_{0.1}O_{3-\delta}$ proton conductors. *J. Power Sources.* **2011**, *196*, 3461-3469.

73. He, T.; Jia, C. L.; Ehrhart, P.; Meuffels, P. On the preparation and microstructure of Y-doped $BaCeO_3$ perovskite thin films. *Solid State Ionics.* **1996**, *89*, 9-12.

74. Hao, X.; Liu, Y.; Wang, Z.; Qiao, J.; Sun, K. A novel sintering method to obtain fully dense gadolinia doped ceria by applying a direct current. *J. Power Sources.* **2012**, *210*, 86-91.

75. Biesuz, M.; Dell'Agli, G.; Spiridigliozzi, L.; Ferone, C.; Sglavo, V. M. Conventional and field-assisted sintering of nanosized Gd-doped ceria synthesized by co-precipitation. *Ceram. Int.* **2016**, *42,* 11766-11771.

76. Jiang, T.; Wang, Z.; Zhang, J.; Hao, X.; Rooney, D.; Liu, Y.; Sun, W.; Qiao, J.; Sun, K. Understanding the flash sintering of rare-earth ceria for solid oxide fuel cells. *J. Am. Ceram. Soc.* **2015**, *98 (6)*, 1717-1723.

77. Spiridigliozzi, L.; Biesuz, M.; Dell'Agli, G.; Di Bartolomeo, E.; Zurlo, F.; Sglavo, V. M. Microstructural and electrical investigation of flash-sintered Gd/Sm-doped ceria. *J. Mater. Sci.* **2017**, *52*, 7479-7488.

78. Valdebenito, J. U.; Akbari-Fakhrabadi, A.; Viswanathan, M. R. Effect of flash sintering on microstructure of $Ce_{0.9}Gd_{0.1}O_{1.95}$ electrolyte fabricated by tape-casting. *Mater. Lett.* **2017**, *209,* 291-294.

79. Glasscock, J. A.; Esposito, V.; Foghmoes, S. P. V.; Stegk, T.; Matuschek, D.; Ley, M. W. H.; Ramousse, S. The effect of forming stresses on the sintering of ultra-fine $Ce_{0.9}Gd_{0.1}O_{2-\delta}$ powders. *J. Eur. Ceram. Soc.* **2013**, *33,* 1289-1296.

80. Li, J.; Guan, L.; Zhang, W.; Luo, M.; Song, J.; Song, X.; An, S. Sintering behaviour of samarium doped ceria under DC electrical field. *Ceram. Int.* **2018**, *44,* 2470-2477.

81. Park, K.; Hwang, H. K.; Choi, J. W. Influence of sintering temperature on $Ce_{0.8}Sm_{0.2}O_{2-\delta}$ for intermediate temperature solid oxide fuel cells. *ECS Meet.* **2010** *Abstr.* MA 2010-02 1386.

82. Pawar, M. J.; Chaure, S. S.; Deshmukh, S. B. Effect of Co co-doping on the densification and electrical conductivity of $Ce_{0.9}Sm_{0.1}O_{2-\delta}$ solid electrolytes. *J. Ceram. Sci. Tech.* **2010**, *1 (1),* 27-31.

83. Han, M.; Liu, Z.; Zhou, S.; Yu, L. Influence of lithium oxide addition on the sintering behaviour and electrical conductivity of gadolinia doped ceria. *J. Mater. Sci. Tech.* **2011**, *27 (5),* 460-464.

84. Kleinlogel, C.; Gauckler, L. J. Sintering of nanocrystalline CeO_2 ceramics. *Adv. Mater.* **2001**, *13 (14),* 1081-1085.

85. Yoshida, H.; Sakka, Y.; Yamamoto, T.; Lebrun, J. M.; Raj, R. Densification behaviour and microstructural development in undoped yttria prepared by flash-sintering. *J. Eur. Ceram. Soc.* **2014**, *34,* 991-1000.

86. Chen, P.-L.; Chen, I.-W. Sintering of fine oxide powders: I, microstructural evolution. *J. Am. Ceram. Soc.* **1996**, *79 (12)*, 3129-3141.

87. Yoshida, H.; Morita, K.; Kim, B.-N.; Sakka, Y.; Yamamoto, T. Reduction in sintering temperature for flash-sintering of yttria by nickel cation-doping. *Acta Mater.* **2016**, *106,* 344-352.

88. Kodo, M.; Soga, K.; Yoshida, H.; Yamamoto, T. Low temperature sintering of polycrystalline yttria by transition metal ion doping. *J. Ceram. Soc. Jpn.* **2009**, *117 (6),* 765-768.

89. Zuo, F.; Badev, A.; Saunier, S.; Goeuriot, D.; Heuguet, R.; Marinel, S. Microwave versus conventional sintering: Estimate of the apparent activation energy for densification of α-alumina and zinc oxide. *J. Eur. Ceram. Soc.* **2014**, *34,* 3103-3110.

90. Zhang, Y.; Jung, J.-I.; Luo, J. Thermal runaway, flash sintering and asymmetrical microstructural development of ZnO and ZnO-Bi$_2$O$_3$ under direct currents. *Scr. Mater.* **2015**, *106,* 26-29.

91. Senda, T. Grain growth in sintered ZnO and ZnO-Bi$_2$O$_3$ ceramics. *J. Am. Ceram. Soc.* **1990**, *73 (1)*, 106-114.

92. Muccillo, E. N. S.; Muccillo, R. Electric field-assisted sintering of tin dioxide with manganese dioxide addition. *J. Eur. Ceram. Soc.* **2014**, *34,* 3699-3706.

93. Muccillo, E. N. S.; Muccillo, R. Electric field-assisted sintering of tin dioxide. *J. Eur. Ceram. Soc.* **2014**, *34,* 915-923.

94. Park, S. J.; Hirota, K.; Yamamura, H. Densification of nonadditive SnO$_2$ by hot isostatic pressing. *Ceram. Int.* **1984**, *10 (3),* 116.

95. Luo, G. Q.; Li, J.; Zhang, D. M.; Shen, Q.; Zhang, L. M. Densification mechanism of SnO$_2$ ceramics doped with 5.0 mol% MnO$_2$. *Key Engineering Materials.* **2007**, *351,* 88-92.

96. M'Peko, J.-C.; Francis, J. S. C.; Raj, R. Field-assisted sintering of undoped BaTiO3: Microstructure evolution and dielectric permittivity. *J. Eur. Ceram. Soc.* **2014**, *34,* 3655-3660.

97. Uehashi, A.; Yoshida, H.; Tokunaga, T.; Sasaki, K.; Yamamoto, T. Enhancement of sintering rates in BaTiO$_3$ by controlling of DC electric current. *J. Ceram. Soc. Jpn.* **2015**, *123 (6),* 465-468.

98. Nakagawa, Y.; Yoshida, H.; Uehashi, A.; Tokunaga, T.; Sasaki, K.; Yamamoto, T. Electric current-controlled synthesis of BaTiO$_3$. *J. Am. Ceram. Soc.* **2017**, *100*, 3843-3850.

99. Cheng, X.; Cui, H.; Xu, Z.; Chen, X.; Wang, Y. Influence of sintering time on the PTCR effect of Nb$_2$O$_5$-doped BaTiO$_3$ ceramics. *Mater. Res.* **2019**, *22 (2)*, 1-5.

100. Kim, D.-H.; Joung, M.-R.; Seo, I.-T.; Hur, J.; Kim, J.-H.; Kim, B.-Y.; Lee, H.-J.; Nahm, S. Influence of sintering conditions on piezoelectric properties of KNbO$_3$ ceramics. *J. Eur. Ceram. Soc.* **2014**, *34,* 4193-4200.

101. Corapcioglu, G.; Gulgun, M. A.; Kisslinger, K.; Sturm, S.; Jha, S. K.; Raj, R. Microstructure and microchemistry of flash sintered K$_{0.5}$Na$_{0.5}$Nb$_3$. *J. Ceram. Soc. Jpn.* **2016**, *124 (4),* 321-328.

102. Feizpour, M.; Bafrooei, H. B.; Hayati, R.; Ebadzadeh, T. Microwave-assisted synthesis and sintering of potassium niobate lead-free piezoelectric ceramics. *Ceram. Int.* **2014**, *40,* 871-877.

103. Su, X.; Bai, G.; Jia, Y.; Wang, Z.; Hu, Y.; Yan, X.; Xie, J. Flash sintering of sodium niobate ceramics. *Mater. Lett.* **2019**, *235,* 15-18.

104. Liu, W. Dielectric and sintering properties of NaNbO$_3$ ceramic prepared by Pechini method. *J. Electroceram.* **2013**, *31,* 376-381.

105. Jesus, L. M.; Silva, R. S.; Raj, R.; M'Peko, J.-C. Electric field-assisted flash sintering of CaCu$_3$Ti$_4$O$_{12}$: microstructure characteristics and dielectric properties. *J. Alloys Compd.* **2016**, *682,* 753-758.

106. Pérez-Maqueda, L. A.; Gil-González, E.; Perejón, A.; Lebrun, J.-M.; Sánchez-Jiménez, P. E.; Raj, R. Flash sintering of highly insulating nanostructured phase-pure BiFeO$_3$. *J. Am. Ceram. Soc.* **2017**, *100*, 3365-3369.

107. Gil-González, E.; Perejón, A.; Sánchez-Jiménez, P. E.; Raj, R.; Pérez-Maqueda, L. A. Processing and properties of Bi$_{0.98}$R$_{0.02}$FeO$_3$ (R = La, Sm, Y) ceramics flash sintered at ~650 °C in <5 s. *J. Am. Ceram. Soc.* **2019**, *103*, 136-144.

108. Moos, R.; Härdtl, K. H. Dependence of the intrinsic conductivity minimum of SrTiO$_3$ ceramics on the sintering atmosphere. *J. Am. Ceram. Soc.* **1995**, *78 (9),* 2569-2571.

109. Lemke, F.; Rheinheimer, W.; Hoffmann, M. J. A comparison of power controlled flash sintering and conventional sintering of strontium titanate. *Scr. Mater.* **2017**, *130,* 187-190.

110. Yan, L. C.; Hassan, J.; Hashim, M.; Yin, W. S.; Khoon, T. F.; Jeng, W. Y. Effect of sintering temperatures on the microstructure and dielectric properties of $SrTiO_3$. *World Appl. Sci. J.* **2011**, *15 (11),* 1614-1618.

111. Lemke, F.; Rheinheimer, W.; Hoffmann, M. J. Sintering and grain growth in $SrTiO_3$: impact of defects on kinetics. *J. Ceram. Soc. Jpn.* **2016**, *124 (4),* 346-353.

112. Straka, W.; Amoah, S.; Schwartz, J. Densification of thoria through flash sintering. *Mater. Res. Soc. Symp. Proc.* **2017**, *7,* 677-682.

113. Ananthasivan, K.; Balakrishnan, S.; Anthonysamy, S.; Divakar, R.; Mohandas, E.; Ganesan, V. Syntesis and sintering of nanocrystalline thoria doped with CaO and MgO derived through oxalate-deagglomeration. *J. Nucl. Mater.* **2013**, *434,* 223-229.

114. Candelario, V. M.; Moreno, R.; Todd, R. I.; Ortiz, A. L. Liquid-phase assisted flash sintering of SiC from powder mixtures prepared by aqueous colloidal processing. *J. Eur. Ceram. Soc.* **2017**, *37,* 485-498.

115. Borrero-López, O.; Pajares, A.; Ortiz, A. L.; Guibertreau, F. Hardness degradation in liquid-phase sintered SiC with prolonged sintering. *J. Eur. Ceram. Soc.* **2007**, *27,* 3359-3364.

116. Muccillo, E. N. S.; Carvalho, S. G. M.; Muccillo, R. Electric field-assisted pressureless sintering of zirconia-scandia-ceria solid electrolytes. *J. Mater. Sci.* **2018**, *53,* 1658-1671.

117. Grasso, R. L.; Muccillo, E. N. S. Sintering, phase composition and ionic conductivity of zirconia-scandia-ceria. *J. Power Sources.* **2013**, *233,* 6-13.

118. Jha, S. K.; Raj, R. The effect of electric field on sintering and electrical conductivity of titania. *J. Am. Ceram. Soc.* **2014**, *97 (2),* 527-534.

119. Chao, S.; Petrovsky, V.; Dogan, F. Effects of sintering temperature on the microstructure and dielectric properties of titanium dioxide ceramics. *J. Mater. Sci.* **2010**, *45,* 6685-6693.

120. Valdez, J. A.; Byler, D. D.; Kardoulaki, E.; Francis, J. S. C.; McClellan, K. J. Flash sintering of stoichiometric and hyper-stoichiometric urania. *J. Nucl. Mater.* **2018**, *505,* 85-93.

121. Raftery, A. M.; da Silva, J. G. P.; Byler, D. D.; Andersson, D. A.; Uberuaga, B. P.; Stanek, C. R.; McClellan, K. J. Onset conditions for flash sintering of UO_2. *J. Nucl. Mater.* **2017**, *493,* 264-270.

122. Kang, K. W.; Yang, J. H.; Kim, J. H.; Rhee, Y. W.; Kim, D. J.; Kim, K. S.; Song, K. W. Effects of $MnO-Al_2O_3$ on the grain growth and high-temperature deformation strain of UO_2 fuel pellets. *J. Nucl. Sci. Technol.* **2010**, *47 (3),* 304-307.

123. Frasnelli, M.; Pedranz, A.; Biesuz, M.; Dirè, S.; Sglavo, V. M. Flash sintering of Mg-doped tricalcium phosphate (TCP) nanopowders. *J. Eur. Ceram. Soc.* **2019**, *39,* 3883-3892.

124. Destainville, A.; Rolo, A.; Champion, E.; Bernache-Assollant, D. Synthesis and characterization of beta tricalcium phosphate. *Key Engineering Materials.* **2003**, *240-242,* 489-492.

125. Avila, V.; Raj, R. Reactive flash sintering of powders of four constituents into a single phase of a complex oxide in a few seconds below 700 °C. *J. Am. Ceram. Soc.* **2019**, *102,* 6443-6448.

126. Xue, W.; Yang, Y.; Yang, Q.; Liu, Y.; Wang, L.; Chen, C.; Cheng, R. The effect of sintering process on lithium ionic conductivity of $Li_{6.4}Al_{0.2}La_3Zr_2O_{12}$ garnet produced by solid-state synthesis. *RSC Adv.* **2018**, *8,* 13083-13088.

127. Mikami, M.; Kinemuchi, Y.; Kubo, K.; Uchiyama, N.; Miyazaki, H.; Nishino, Y. Near-net-shape fabrication of thermoelectric legs by flash sintering. *J. Electron. Mater.* **2020**, *49 (1),* 593-600.

128. Mikami, M.; Matsumoto, A.; Kobayashi, K. Synthesis and thermoelectric properties of microstructural Heusler Fe_2Val alloy. *J. Alloys Compd.* **2008**, *461,* 423-426.

9. ACRONYMS

3YSZ: 3 mol% yttria-stabilized-zirconia

8YSZ: 8 mol% yttria-stabilized-zirconia

TZP: tetragonal zirconia

10GDC: 10 mol% gadolinium-doped ceria

KNN: potassium sodium niobium oxide

10Sc1CeSZ: zirconia doped with 10 mol% scandia and 1 mol% ceria

TCP: tricalcium phosphate

APPENDICES

APPENDIX 1: CONVENTIONAL AND FLASH SINTERING CONDITIONS

Entry	Compound	Flash-sintering				Conventional sintering		
		Author	Temperature (°C)	Applied field (V/cm)	Time (s)	Author	Temperature (°C)	Time (h)
1	3YSZ	Cologna (2010) [2]	850	120	<5	Ji (2017) [54]	1315	1
2		Ji (2017) [54]	925	150	<30			
3		Carvalho (2018) [55]	1000	200	300			
4		Liu (2020) [56]	700	150	15			
5	20 vol.% Al_2O_3-3YSZ	M'Peko (2020) [57]	815	150	few seconds	Azhar (2009) [58]	1600	4
6	8YSZ	Muccillo (2011) [59]	964	16	60	Dahl (2007) [63]	1150-1300	1
7		Muccillo (2013) [9]	800	80	few seconds			
8		Downs (2013) [60]	390	2250	few seconds			
9		Steil (2013) [61]	975	80	165			
10		Muccillo (2014) [62]	800	120	1800			

11	Co_2MnO_4	Prette (2011) [64]	325	12.5	few seconds	Prette (2011) [65]	1100	several hours
12	0.25 wt.% $MgO-Al_2O_3$	Cologna (2011) [8]	1260	1000	few seconds	Zhao (1987)[(1)] [66]	1620	3
13	60 vol.% Al_2O_3-TZP	Bichaud (2015) [15]	1100	200	N/A	Bichaud (2015) [15]	1500	no dwell time
14	Al_2O_3	Biesuz (2018) [67]	1200	1000	few seconds	Pulgarín (2015) [68]	1500	2
15	$BaCe_{0.8}Gd_{0.2}O_{3-\delta}$	Muccillo (2012) [69]	910	40	5	Maffei (2004) [70]	1650	10
16	$BaCe_{0.9}Gd_{0.1}O_{3-\delta}$	Muccillo (2018) [71]	1200	200	300	Amsif (2011) [72]	1400	4
17	$BaCe_{0.9}Sm_{0.1}O_{3-\delta}$	Muccillo (2018) [71]	1200	200	300			
18	$BaCe_{0.9}Y_{0.1}O_{3-\delta}$	Muccillo (2018) [71]	1200	200	300	He (1996) [73]	1450	40
19	$Ce_{0.8}Gd_{0.2}O_{1.8}$	Hao (2012) [74]	545	70	few seconds	Hao (2012) [74]	1570	6
20		Biesuz (2016) [75]	565	150	60			
21		Jiang (2015) [76]	554	90	600			
22		Spiridigliozzi (2017) [77]	~400	250	30-60			
23	$Ce_{0.9}Gd_{0.1}O_{1.9}$	Valdebenito (2017) [78]	600	100	300	Glasscock (2013) [79]	1500	no dwell time
24		Jiang (2015) [76]	635	90	600			
25		Spiridigliozzi (2017) [77]	~450	250	30-60			

26	$Ce_{0.8}Sm_{0.2}O_{1.9}$	Jiang (2015) [76]	667	90	600	Park (2010) [81]	1200-1450	4
27		Li (2018) [80]	578	120	60			
28	$Ce_{0.9}Sm_{0.1}O_{1.9}$	Spiridigliozzi (2017) [77]	~400	250	30-60	Pawar (2010) [82]	1550	7
29	1 mol% Li_2O-10GDC	Spiridigliozzi (2017) [77]	~400	150	30-60	Han (2011)[(2)] [83]	750	4
30	1 mol% CoO-10GDC	Spiridigliozzi (2017) [77]	~500	250	30-60	Kleinlogel (2001) [84]	840	2
31	Y_2O_3	Yoshida (2014) [85]	985	1000	<10	Chen (1996) [86]	1500-1700	12
32	1 mol% Ni^{2+}-Y_2O_3	Yoshida (2016) [87]	823	1000	N/A	Kodo (2009) [88]	1200-1600	3
33	ZnO	Schmerbauch (2014) [25]	623	300	30	Zuo (2014) [89]	1050	no dwell time
34		Zhang (2015) [24]	116[(3)]	1000	~30			
35		Zhang (2015) [90]	553	300	30			
36	0.5 mol% Bi_2O_3-ZnO	Zhang (2015) [90]	620	300	30	Senda (1990) [91]	1030-1400	1-10
37	SnO_2	Muccillo (2014) [92]	1100	110	300	Park (1984) [94]	1400[(4)]	12
38		Muccillo (2014) [93]	900	800	300			
39	1 mol% MnO_2-SnO	Muccillo (2014) [92]	985	110	300	Luo (2007)[(5)][95]	1100	5
40	$BaTiO_3$	M'Peko (2014) [96]	688	500	<60	Cheng (2019)[(6)][99]	1190	0.5-6
41		Uehashi (2015) [97]	1020	100	60			
42		Nakagawa (2017) [98]	1070	100	5			
43	$KNbO_3$	Shomrat (2015) [29]	750	600	330	Kim (2014) [100]	1020	6

44	KNN	Corapcioglu (2016) [101]	990	250	30	Feizpour (2014) [102]	950	several hours
45	$NaNbO_3$	Su (2019) [103]	862	700	3	Liu (2013) [104]	1150-1245	4
46	$La_{0.8}Sr_{0.2}Ga_{0.8}Mg_{0.2}O_{3-\delta}$	Sun (2016) [32]	672	120	600	Huang (1996)[7][33]	1370[8]	36
47	$CaCu_3Ti_4O_{12}$	Jesus (2016) [105]	750	60	N/A	Jesus (2016) [105]	1050	N/A
48	$BiFeO_3$	Pérez-Maqueda (2017) [106]	~400	150	15	Jeon (2012) [35]	800	12
49	$Bi_{0.98}R_{0.02}FeO_3$	Gil-González (2019) [107]	~650	50	<5			
50	$SrTiO_3$	Shomrat (2017) [23]	850	600	~1200	Moos (1995) [108]	1400	10
51		Lemke (2017) [109]	1120	500	~1800	Yan (2011) [110]	1200	10
52	$SrTi_{0.97}Fe_{0.03}O_{2.985}$	Shomrat (2017) [23]	~620	600	N/A	Lemke (2016)[9] [111]	1280	2-4
53	ThO_2	Straka (2017) [112]	950	800	10	Ananthasivan (2013) [113]	1800	N/A
54	10 wt.% $Y_3Al_5O_{12}$-SiC	Candelario (2017) [114]	900[10]	10 A	50	Borrero-López (2007) [115]	1950[11]	1-7
55	10Sc1CeSZ	Muccillo (2018) [116]	1020	150	120-300	Grasso (2013) [117]	1200	2
56	TiO_2	Charalambous (2018) [10]	500	50	60	Chao (2010) [119]	780	12
57		Jha (2014) [118]	640	1000	few seconds			
58	$UO_{2.00}$	Valdez (2018) [120]	600	188	185	Kang (2010) [122]	1750	N/A
59		Raftery (2017) [121]	26	~110	60			

60	$UO_{2.08}$	Raftery (2017) [121]	26	~30	15			
61	$UO_{2.16}$	Valdez (2018) [120]	600	188	123			
62		Raftery (2017) [121]	26	~15	<10			
63	TCP	Frasnelli (2019) [123]	889	1000	~2400	Destainville (2003) [124]	900-1100[(12)]	0.5
64	5 mol% Mg-TCP	Frasnelli (2019) [123]	860	1000	~2350	Bandyopadhyay (2007)[(13)][124]	1250	3
65	$Li_{5.95}La_3Zr_2Al_{0.35}O_{12}$	Avila (2019) [125]	682	50	10	Xue (2018) [126]	1100-1230	10-20
66	$Li_{6.25}La_3Zr_2Al_{0.25}O_{12}$	Clemenceau (2019) [30]	850	40	few seconds	Murugan (2007) [31]	1230	36
67	Fe_2VAl	Mikami (2020) [127]	27	1.2 kA	0.5	Mikami (2007) [128]	900-1000	several hours

1) 250 ppm $MgO-Al_2O_3$, 2) 1.5 mol% Li_2O-10GDC, 3) Air + 5 mol% H_2, 4) 150 MPa, 5) 5 mol% MnO_2-SnO, 6) $Ba_{1.006}(Ti_{1-x}Nb)O_3$, 7) $La_{0.9}Sr_{0.1}Ga_{0.8}Mg_{0.2}O_{2.85}$, 8) 120 MPa, 9) 2 mol% Fe-$SrTiO_3$, 10) Ar + gas atmosphere, 11) 350 MPa + Ar or N_2 atmosphere, 12) 20 MPa, 13) 2.5 wt.% Mg-TCP.